Interferenceless coded aperture correlation holography for five-dimensional imaging of 3D space, spectrum and polarization

Journal of Physics: Photonics

PAPER

Interferenceless coded aperture correlation holography for five-dimensional imaging of 3D space, spectrum and polarization

Narmada Joshi[1,6], **Vipin Tiwari**[1,6], **Tauno Kahro**[1], **Agnes Pristy Ignatius Xavier**[1,2], **Tatsuki Tahara**[3], **Aarne Kasikov**[1], **Kaupo Kukli**[1], **Saulius Juodkazis**[4,5], **Aile Tamm**[1], **Joseph Rosen**[2] and **Vijayakumar Anand**[1,4,*]

[1] Institute of Physics, University of Tartu, W. Ostwaldi 1, 50411 Tartu, Estonia
[2] School of Electrical and Computer Engineering, Ben Gurion University of the Negev, PO Box 653, Beer-Sheva 8410501, Israel
[3] Applied Electromagnetic Research Center, Radio Research Institute, National Institute of Information and Communications Technology (NICT), 4-2-1 Nukuikitamachi, Koganei, Tokyo 184–8795, Japan
[4] Optical Sciences Center Swinburne University of Technology, Hawthorn, Melbourne VIC 3122, Australia
[5] Tokyo Tech World Research Hub Initiative (WRHI), School of Materials and Chemical Technology, Tokyo Institute of Technology, 2-12-1, Ookayama, Meguro-ku, Tokyo 152-8550, Japan
[6] These authors contributed equally to the manuscript.
[*] Author to whom any correspondence should be addressed.

E-mail: vijayakumar.anand@ut.ee

Keywords: incoherent holography, coded aperture imaging, polarization, 5D imaging

OPEN ACCESS

RECEIVED
17 July 2024

REVISED
15 December 2024

ACCEPTED FOR PUBLICATION
12 January 2025

PUBLISHED
6 February 2025

Abstract

Interferenceless coded aperture correlation holography (I-COACH) is a robust imaging technique for recovering three-dimensional object information using incoherent holography without two-beam interference. In this study, five-dimensional (5D) imaging along 3D space, spectrum and polarization in I-COACH is proposed and experimentally demonstrated for the first time. The proposed technique exploits the polarization-dependent light modulation characteristics of spatial light modulators to record polarization-dependent intensity distributions, which are distinguished by significant blurring between orthogonal polarization states. 5D I-COACH is implemented by inter-connecting all five dimensions in a single frame, and image recovery is attempted from different configurations of recorded point spread intensity distributions and response-to-object intensity distributions along 5D using recently developed deconvolution techniques. The simulation and experimental results confirm the 5D imaging capabilities of I-COACH. The proposed technique can be a useful tool for birefringence microscopy, and functional and structural imaging applications.

1. Introduction

Interferenceless coded aperture correlation holography (I-COACH) was developed in 2017 to record and reconstruct 3D information without two beam interference using spatially incoherent illumination [1]. The development of I-COACH had a significant impact on the area of incoherent digital holography (IDH) [2–5], as two-beam interference was one irreplaceable requirement in IDH before the development of I-COACH. In IDH, light from an object point is split into two parts, differently modulated and interfered with, to create a self-interference hologram [6, 7]. In all the IDH studies [2], the mathematical relations between the object and the hologram were either through Fresnel or Fourier integrals [8]; therefore, the object can be reconstructed from the hologram by the above-mentioned numerical versions in a computer. Since the IDH configurations were predominantly inline, at least three camera recordings with phase-shifted modulations were required to reconstruct the object information without reconstruction noise. In I-COACH, the light from an object is modulated by an amplitude or phase coded mask (CM), and the resulting intensity distribution is recorded. The image of the object is reconstructed by processing the response-to-object intensity distribution with a point spread function (PSF) recorded under conditions identical to those used for the object. This processing can occur through one of the many deconvolution methods developed for

coded aperture imaging methods and image deblurring methods [9–18]. Consequently, a single shot was easily achievable in I-COACH, unlike in IDH. In early studies [1, 19–21], the choice of CMs was limited to only scattering masks, similar to only lenses in IDH. Later, I-COACH was adapted to various types of masks and PSF distributions [22–25]. The above flexibility further expanded the capabilities of I-COACH in comparison to IDH, resulting in unconventional imaging characteristics. For instance, in IDH, the images are reconstructed exactly as if a lens in direct imaging mode images them but digitally in the computer, resulting in imaging with the characteristics of a lens. With the Fresnel incoherent correlation holography configuration, there is a unique behavior of high lateral and low axial resolution, but it is fixed [3, 6]. With I-COACH and different masks, such as cubic phase masks, interesting imaging characteristics, such as shifting the image locations with respect to axial locations on demand, became possible [24].

An interesting direction along which I-COACH evolved was recording information along multiple dimensions within one or a few camera shots. The spectral imaging method was demonstrated using a diffuser to record 2D spatial information along the spectrum [26]. Four-dimensional imaging along 3D space and spectrum was demonstrated with COACH, a precursor of I-COACH in the framework of IDH, using a monochrome camera [27] and later using I-COACH [28] and a similar technique with spectral filter arrays [29]. The inclusion of additional dimensions in the same hologram was not without challenges. In the lensless I-COACH case [28], undesirable depth-wavelength reciprocity was observed, causing confusion between changes in depth and wavelength. In [29], such challenges were not presented because a spectral filter array was used for wavelength discrimination.

Another useful imaging dimension is the polarization, which can reveal valuable information about the specimen [30–33]. Polarization imaging has many advantages, such as reduced scattering noise, birefringence measurement, and information multiplexing [30–33]. However, the implementation of polarization imaging is quite challenging, and the outcomes often follow the same trend of intensity variation with respect to the polarization angle. To extend polarization imaging to holography, polarization-dependent defocusing is desirable. Recently, polarization-sensitive imaging was demonstrated in the IDH region to map polarization with intensity [34]. Another straightforward approach is to create a polarization-dependent PSF [35, 36].

Due to an increase in demand for advanced imaging capabilities, multidimensional information composed of polarization and stereo vision has been developed [37]. In recent years, 4D imaging systems based on IDH have also been developed [38, 39]. In a few camera shots, multiple holograms were recorded based on the principles of IDH, and depth-specific and polarization-specific information was reconstructed. In polarization imaging methods, changes in polarization often translate to changes in intensity [34]. In [38, 39], for the first time, polarization changes were successfully translated to blur, allowing the encoding and decoding of both space and polarization information in a single hologram. However, one of the challenges in the above studies [38, 39] is that the procedure requires multiple camera recordings, which precludes recording dynamic scenes. Another challenge is that the above methods require at least two liquid crystal devices, such as spatial light modulators (SLMs), which increases the cost of the imaging system. The final challenge is that the polarization discrimination observed as a blur is not significant.

In this study, we proposed and demonstrated five-dimensional (5D) imaging along 3D space, spectrum and polarization in I-COACH for the first time. The above 5D imaging is implemented in a single camera shot given that an extensive PSF library along depth, wavelength and polarization has been recorded once and stored in the computer. Therefore, the presented imaging technology can be called 6D I-COACH because time can be the sixth dimension, with no reduction in the temporal resolution of the camera, as with other holographic techniques. The proposed 6D I-COACH requires only one SLM and can show significant polarization discrimination, as indicated by massive blurring between the orthogonal states. The above advantages make 6D I-COACH a desirable imaging tool for advanced imaging applications. The manuscript consists of five sections. The methodology is presented in the next section. The simulation studies are presented in the third section. The fabrication of the diffractive optical element (DOE) is discussed in the fourth section. The imaging experiments and results are presented in the fifth section. The conclusion and future perspectives are presented in the final section.

2. Methodology

Only spatially incoherent light illumination is considered in this study, as with previous studies on I-COACH. The optical configuration is shown in figure 1. Light from an object is incident on a coded phase mask (CPM) displayed on a SLM. A 4*f* system comprising two refractive lenses with the same focal length *f* projects the complex amplitude after the SLM on an amplitude-type DOE. The light modulated by the DOE is recorded by a monochrome image sensor. One-time calibration of the system was carried out by recording the PSF library for different conditions of depth, wavelength and polarization, and the data were stored on a computer. Then, a multidimensional object with variations in depth, wavelength and polarization is

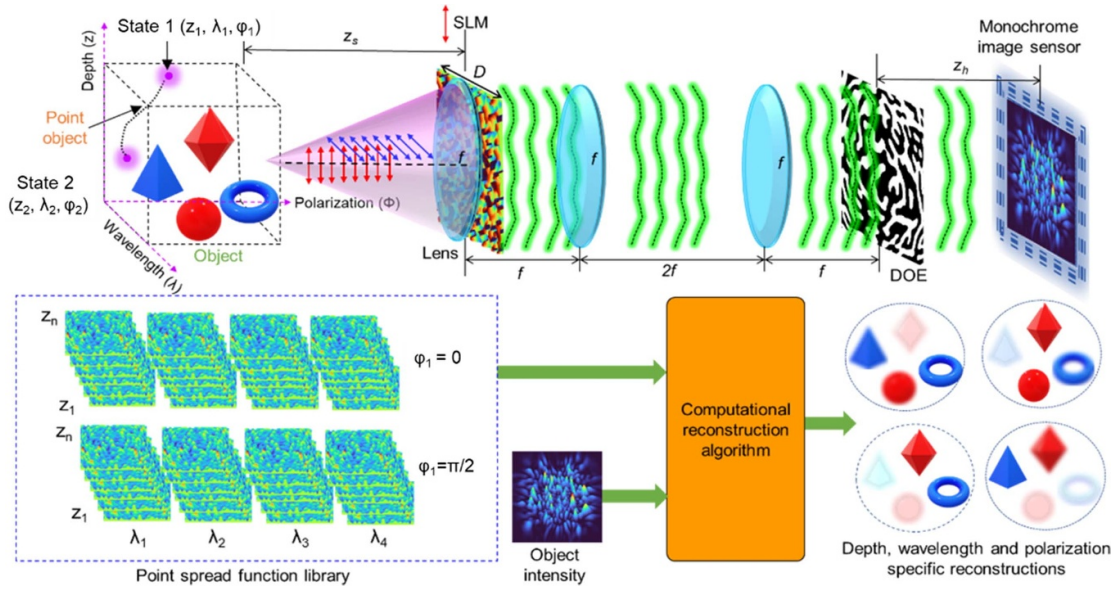

Figure 1. Schematic of 5D-I-COACH.

mounted within the calibrated multidimensional space along the above three parameters, and a single camera shot is recorded. One of the computational deconvolution methods [18] is applied to the PSF library, and the response-to-object intensity pattern and multidimensional information of the object are reconstructed.

Let us consider a point object with an amplitude of $\sqrt{I_s}$ located at a distance of z_s from a refractive lens with a focal length of f. The complex amplitude after the lens is $\sqrt{I_s}C_1 L\left(\frac{\bar{r}_s}{z_s}\right) Q\left(\frac{1}{z_s}\right) Q\left(-\frac{1}{f}\right)$, where $Q(b) = \exp\left[\mathrm{i}\pi b\lambda^{-1}\left(x^2+y^2\right)\right]$ and $L\left(\frac{\bar{s}}{z}\right) = \exp\left[\mathrm{i}2\pi\left(\lambda z\right)^{-1}\left(s_x x + s_y y\right)\right]$ are the quadratic and linear phase functions, respectively, and C_1 is a complex constant. On the SLM, a CPM with a phase of $(\exp(\mathrm{i}\Phi_{\mathrm{CPM}}))$ is displayed. There are two possible outcomes for the two orthogonal polarizations. For the first case, when the polarization is along the active axis of liquid crystal based SLM, and $\varphi = 0$, the complex amplitude after the SLM is given as $\sqrt{I_s}C_1 L\left(\frac{\bar{r}_s}{z_s}\right) Q\left(\frac{1}{z_s}\right) Q\left(-\frac{1}{f}\right) \exp(\mathrm{i}\Phi_{\mathrm{CPM}})$. The above complex amplitude is projected through a $4f$ system on an amplitude-type DOE with an amplitude distribution of $M(x,y)$ fabricated using a lithography technique. The complex amplitude after the DOE is therefore given as $\sqrt{I_s}M(x,y)\,C_1 L\left(\frac{\bar{r}_s}{z_s}\right) Q\left(\frac{1}{z_s}\right) Q\left(-\frac{1}{f}\right) \exp(\mathrm{i}\Phi_{\mathrm{CPM}})$. For the second case, when the polarization is orthogonal to the active axis of the SLM, and $\varphi = \pi/2$, the complex amplitude after the DOE is given as $\sqrt{I_s}M(x,y)\,C_1 L\left(\frac{\bar{r}_s}{z_s}\right) Q\left(\frac{1}{z_s}\right) Q\left(-\frac{1}{f}\right)$. Therefore, there are two different outputs corresponding to two orthogonal polarization cases. The I_{PSF}s for orthogonal polarizations are given as

$$I_o(\bar{r}_0;\bar{r}_s,z_s,\lambda,\varphi) = \left|\sqrt{I_s}C_1 M(x,y)\,L\left(\frac{\bar{r}_s}{z_s}\right) Q\left(\frac{1}{z_s}\right) Q\left(-\frac{1}{f}\right) \exp(\mathrm{i}\Phi_{\mathrm{CPM}}) \otimes Q\left(\frac{1}{z_h}\right)\right|^2 \cos(\varphi) + \left|\sqrt{I_s}C_1 M(x,y)\,L\left(\frac{\bar{r}_s}{z_s}\right) Q\left(\frac{1}{z_s}\right) Q\left(-\frac{1}{f}\right) \otimes Q\left(\frac{1}{z_h}\right)\right|^2 \sin(\varphi) \quad (1)$$

where '$\otimes$' is a 2D convolutional operator. Since the proposed system is a linear, shift-invariant system, the PSF can be expressed as

$$I_{\mathrm{PSF}}(\bar{r}_0;z_s,\lambda,\varphi) = Io\left(\bar{r}_0 - \frac{z_h}{z_s}\bar{r}_s;0,z_s,\lambda,\varphi\right), \quad (2)$$

where z_h/z_s is the magnification of the system.

Let us consider a 2D object consisting of N points. The object can be mathematically expressed as a collection of delta functions as

$$o(\bar{r}_s) = \sum_q^N a_q \delta\left(\bar{r} - \bar{r}_{s,q}\right). \quad (3)$$

The response-to-object intensity distribution can be given as

$$I_{\mathrm{o}}\left(\bar{r}_0; z_s, \lambda, \varphi\right) = \sum_{q}^{N} a_q I_{\mathrm{PSF}}\left(\bar{r}_0 - \frac{z_h}{z_s}\bar{r}_{s,q}; z_s, \lambda, \varphi\right). \tag{4}$$

Considering a multidimensional object and spatial incoherence, the recorded intensity distribution is given as

$$I_{\mathrm{o}}\left(\bar{r}_0\right) = \sum_{k_1,k_2,k_3} I_o\left(\bar{r}_0; z_{sk_1}, \lambda_{k_2}, \varphi_{K_3}\right). \tag{5}$$

Here, k_1, k_2, k_3 are indices that run over the number of depths, wavelengths, and polarization states respectively. The object information corresponding to the depth, wavelength and polarization is reconstructed by processing the total response-to-object intensity distribution, as shown in equation (5), with the corresponding PSF $I_{\mathrm{PSF}}\left(\bar{r}_0; z_s, \lambda, \varphi\right)$. This can be achieved through one of the deconvolution methods. Here, we use two of the recently developed algorithms namely Lucy–Richardson–Rosen algorithm (LRRA) [17] and incoherent non-linear deconvolution using an iterative algorithm (INDIA) [18]. Detailed descriptions of LRRA and INDIA are provided in [17] and [18] respectively. The rationale for choosing LRRA and INDIA over other reconstruction methods such as Weiner deconvolution is based on the outcome of a recent comparison study between different image reconstruction methods for a wide range of deterministic and random masks [18]. In [18], it can be found that LRRA and INDIA performed better than existing algorithms for a wide range of CMs. The reconstructed image is given as

$$I_{\mathrm{R}}\left(p\right) = I_{\mathrm{R}}\left(p-1\right)\left[\frac{I_o}{I_{\mathrm{R}}\left(p-1\right) \otimes I_{\mathrm{PSF}}} *_{\beta}^{\alpha} I_{\mathrm{PSF}}\right], \tag{6}$$

where '$*_{\beta}^{\alpha}$' is the non-linear correlation operator given as $u *_{\beta}^{\alpha} v = \mathcal{F}^{-1}\left\{|U|^{\alpha}|V|^{\beta}\exp\left(i\Phi_U\right).\exp\left(-\mathrm{i}\Phi_V\right)\right\}$, where U and V are the Fourier transforms of u and v, respectively. Since any changes in z_s, λ and φ cause a change in the intensity distribution, a sharp correlation function with a high correlation value can be obtained only when all the conditions are matched. When any one of the three parameters is changed, the correlation value and the sharpness of the correlation function decrease. Consequently, only the object information that is matched with the reconstruction function is strongly and sharply reconstructed, while the other object information corresponding to other conditions appears blurred and weak.

3. Simulation studies

The simulation study was carried out using MATLAB software. A pixel size of $\Delta = 10$ μm, a matrix size of 500×500 pixels and a simulation wavelength of $\lambda = 650$ nm were used for the optical configuration with $z_s = z_h = 40$ cm. The focal length of the refractive lens after the object is $f = 40$ cm. Two diffractive functions, one for phase modulation on an SLM and the other for amplitude modulation, were selected. For the phase diffractive function on the SLM, a spiral lens (SLs) given as $\exp[-i\pi\left(\lambda f\right)^{-1}r^2] \times \exp\left(-\mathrm{i}L\theta\right)$, where $r = \left(x^2+y^2\right)^{1/2}$, $\tan\left(\theta\right) = y/x$ and L is the topological charge, which is set at 5, is selected. For the amplitude diffractive element, a binarized version of the quasi-random diffractive lens (QRDL) given as $\left(\exp[-i\pi\left(\lambda f\right)^{-1}r^2] \times exp\left[i\Phi_{\sigma}\left(x,y\right)\right]\right)$ is selected, where σ is the scattering degree of the quasi-random phase function Φ, and following binarization, the values of the mask are 0 or 1. It must be noted it is not mandatory to have the above two diffractive functions at the SLM and the DOE respectively for the demonstration of 5D I-COACH. The goal is to obtain maximum discrimination between orthogonal polarization states in addition to having a high throughput from the object to the image sensor which is desirable for any imaging system. Case—1, when the light from the object is polarized along the active axis of the SLM, it undergoes two modulations, one at the SLM and another at the DOE. Case—2, when the light from the object is polarized orthogonal to the active axis of the SLM, the light from the object undergoes only one modulation which is at the DOE. In principle, even if same diffractive functions are used at the SLM and the DOE, the resulting intensity distributions will be different for the two orthogonal polarization cases. In this study, we chose a SLs with a topological charge $L = 5$ and a binary random lens as this combination enables maximum discrimination between the two polarization states in simulation and experiments. The design algorithm of the QRDL is shown in figure 2. The goal is to design an amplitude-only QRDL with controlled scattering and a focal length where the scattered pattern has the smallest area. This design is achieved using the Gerchberg–Saxton algorithm (GSA) [40]. Two planes, namely, the CM plane and sensor

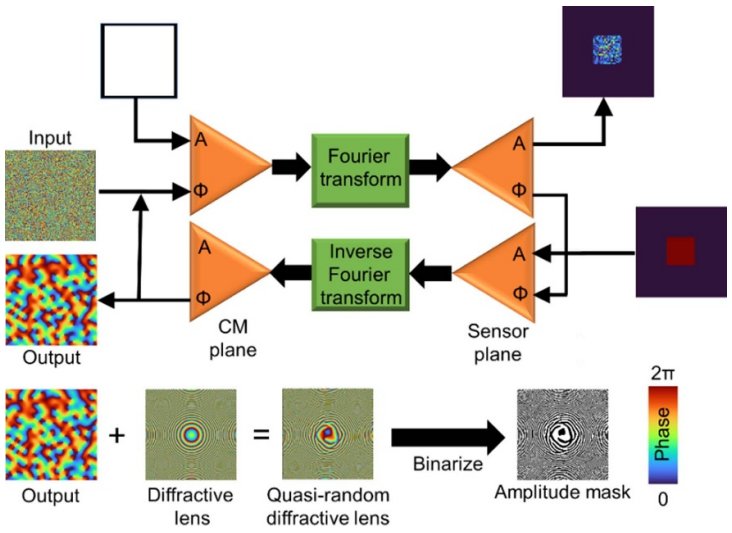

Figure 2. Schematic of the GSA for the design of the QRDL.

plane, connected by a Fourier transform operation are considered. A phase-only constraint is set at the CM plane, where the amplitude function is set to a matrix with all values 1 and the phase matrix is calculated iteratively. At the sensor plane, a limited support constraint is applied to the amplitude matrix while the phase is calculated. The complex amplitudes at the two planes are Fourier transformed in the forward iteration and inverse Fourier transformed in the backward iteration. After several iterations (∼50), the phase matrix at the CM plane converges to a stable pattern, which is binarized and used as an amplitude-only QRDL. The two elements for phase and amplitude modulation by an active device (SLM) and passive element fabricated by lithography, respectively, can be any diffractive elements. The current choice of diffractive functions and configuration was based on the requirement of achieving a speckle pattern with sharp speckles at the sensor plane. The 4-f system shown in figure 1 transfers the phase-only diffractive function of the SLM to the amplitude-only diffractive function, resulting in a complex modulation function.

Two test objects, namely, the CIPHR logo (Object 1) and the logo of University of Tartu (Object 2), were used as the test objects for the two polarization states $\varphi = 0$ and $\pi/2$, as shown in figures 3(a) and (b), respectively. The phase and amplitude images of the two diffractive functions are shown in figures 3(c) and (d), respectively. The $I_{\mathrm{PSF}}s$ for $\varphi = 0$ and $\pi/2$ are calculated when both functions are activated and only the amplitude function is activated, as shown in figures 3(e) and (f), respectively. The response-to-object intensity distributions $I_{\mathrm{O}}(\varphi = 0)$ and $I_{\mathrm{O}}(\varphi = \pi/2)$ of Object 1 with $I_{\mathrm{PSF}}(\varphi = 0)$ and of Object 2 with $I_{\mathrm{PSF}}(\varphi = \pi/2)$ are shown in figures 3(g) and (h), respectively. The reconstruction results obtained by processing $I_{\mathrm{O}}(\varphi = 0)$ with $I_{\mathrm{PSF}}(\varphi = 0)$, $I_{\mathrm{O}}(\varphi = \pi/2)$ with $I_{\mathrm{PSF}}(\varphi = \pi/2)$, $I_{\mathrm{O}}(\varphi = 0)$ with $I_{\mathrm{PSF}}(\varphi = \pi/2)$, and $I_{\mathrm{O}}(\varphi = \pi/2)$ with $I_{\mathrm{PSF}}(\varphi = 0)$ are shown in figures 3(i)–(l), respectively. I-COACH has already been studied thoroughly for other dimensions, namely, depth and wavelength, in previous studies, so only simulation studies for polarization discrimination have been conducted [28].

4. Fabrication of the passive DOE

A schematic of the fabrication process of the QRDL is shown in figure 4(a). The QRDL was fabricated by photolithography in an ISO5 clean room. In the first step, the positive photoresist (AR-P 3510T, Allresist, Strausberg, Germany) was spin-coated (4000 rpm, 60 s) with a thickness of 2.2 μm onto BaF_2 substrates and then softly baked on a hot plate at 100 °C for 60 s to decrease the remaining solvent content and improve photoresist adhesion to the substrate. The promoter AR 300–80 new (∼15 nm) (Allresist, Strausberg, Germany) was used to enhance the adhesion-promoting effect between the photoresist and the BaF_2 substrates. Furthermore, the photoresist was exposed by a Maskless Aligner (Heidelberg Instruments μMLA, Heidelberg, Germany) with a dose control of the light source, and AR 300–44 (Allresist, Strausberg, Germany) was used to develop the UV-irradiated structures. The unwanted residuals were removed by using ultrapure water. Before metallization, the surface of BaF_2 was treated with oxygen plasma for 4 min. Furthermore, Ti (with a thickness of 6 nm) and Au (with a thickness of 100 nm) were electron beam evaporated at room temperature in a vacuum process of approximately 2×10^{-6} mbar with a growth rate of ∼2 Å s^{-1}. A thin Ti layer was used to improve the adhesion between the Au and the BaF_2 substrate. Finally,

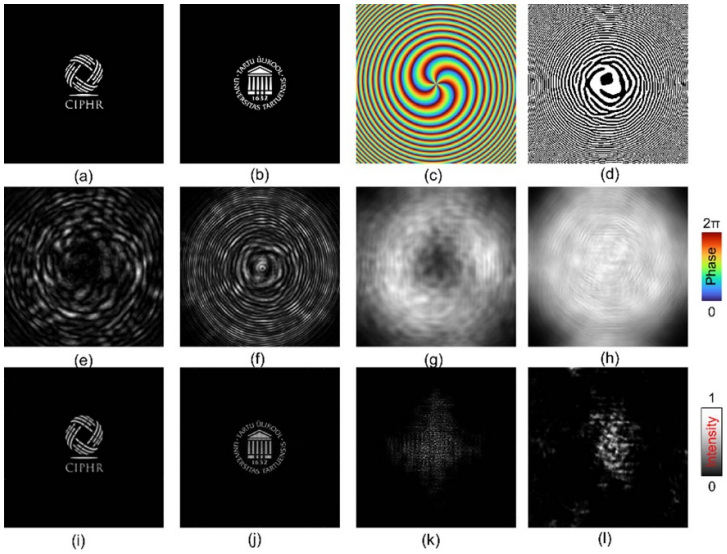

Figure 3. (a) Object 1, (b) Object 2, (c) phase-only mask, (d) amplitude-only mask, (e) I_{PSF} ($\varphi = 0$), (f) I_{PSF} ($\varphi = \pi/2$), (g) I_O ($\varphi = 0$), (h) I_O ($\varphi = \pi/2$), reconstruction result of processing (i) I_{PSF} ($\varphi = 0$) and I_O ($\varphi = 0$), (j) I_{PSF} ($\varphi = \pi/2$) and I_O ($\varphi = \pi/2$), (k) I_{PSF} ($\varphi = 0$) and I_O ($\varphi = \pi/2$) and (l) I_{PSF} ($\varphi = \pi/2$) and I_O ($\varphi = 0$).

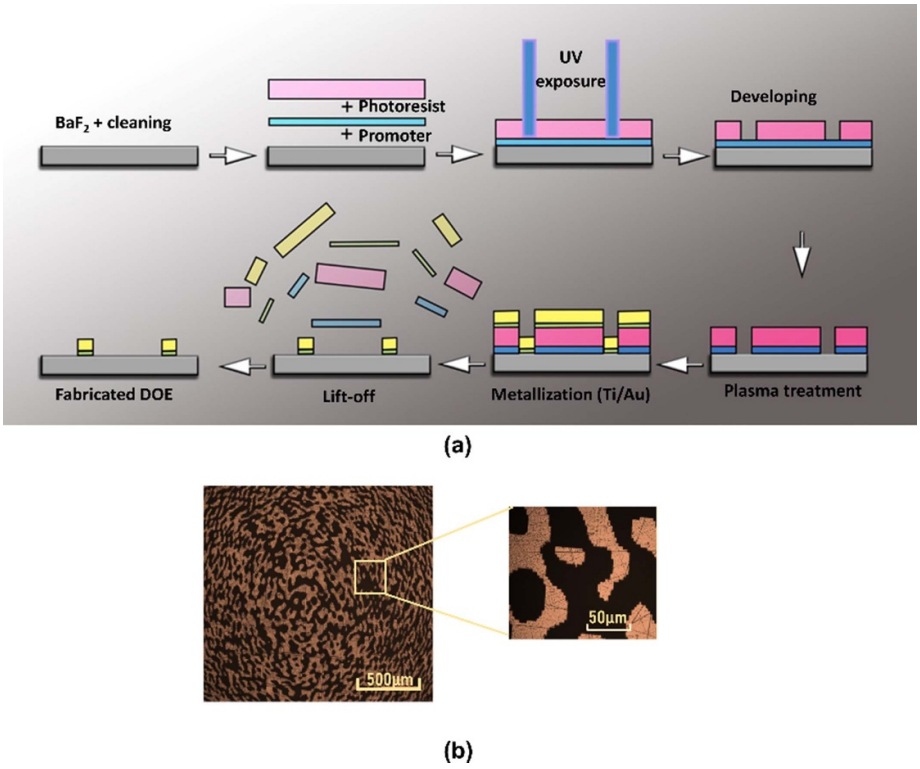

Figure 4. (a) Schematic of the fabrication process of a QRDL on a BaF_2 substrate. (b) Microscopy image of the fabricated QRDL. The inset shows a magnified version of the highlighted region of the QRDL. QRDL—Quasi-random diffractive lens.

the lift-off procedure was carried out in an ultrasonic bath filled with warm acetone to remove excess metal and photoresist; therefore, a QRDL was fabricated for the experiment. Polarized optical microscopy images of the fabricated QRDL on the BaF_2 substrate are shown in figure 4(b). BaF_2 was selected because of its broad range of applicability from visible to infrared wavelengths.

5. Experiments

A schematic and photograph of the experimental configuration of 5D I-COACH are shown in figures 5(a) and (b), respectively. A green light beam coming out from a high-power green LED (Thorlabs, 480 mW,

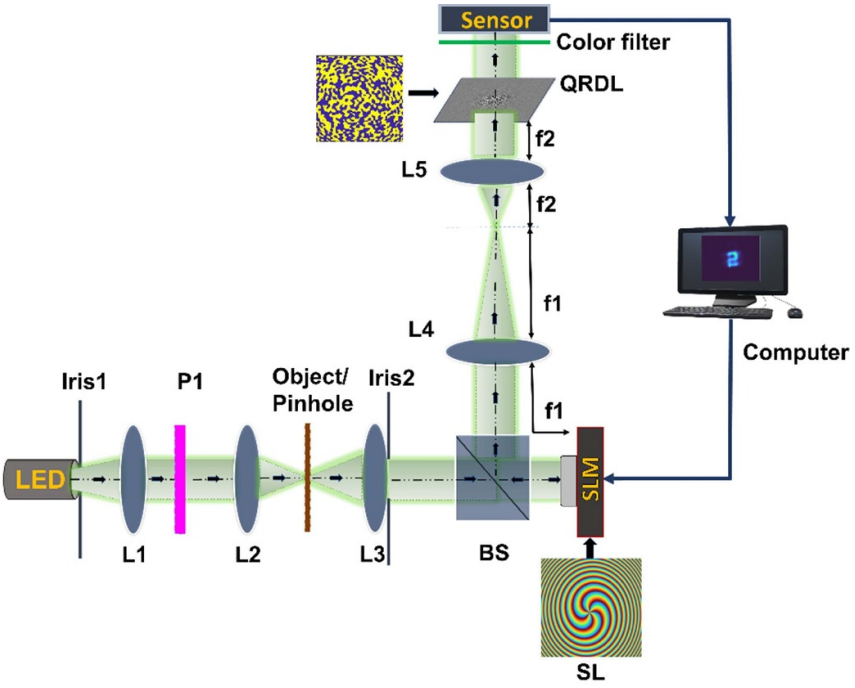

(a)

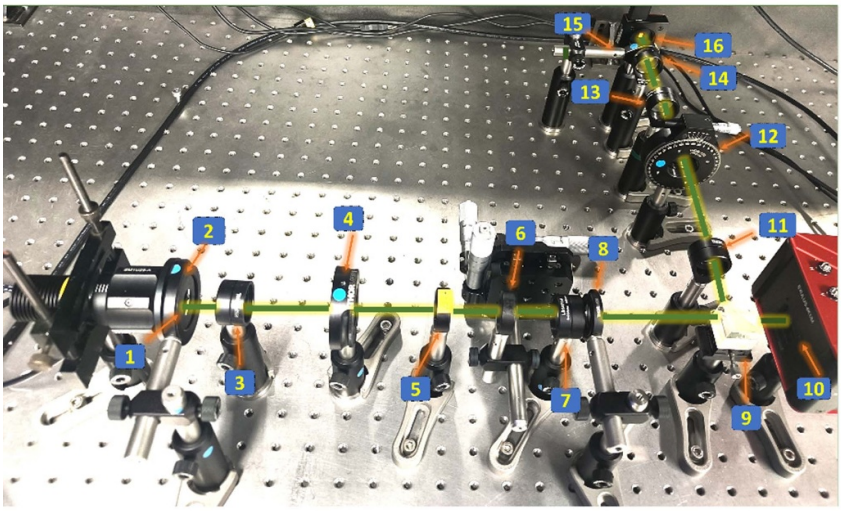

(1) LED, (2) iris1, (3) refractive lens (L1), (4) polarizer(P1), (5) refractive lens (L2), (6) object/pinhole, (7) refractive lens (L3), (8) iris2, (9) beam splitter, (10) SLM, (11) refractive lens (L4), (12) aperture, (13) refractive lens (L5),(14) QRDL:quasi random diffractive lens, (15) color filter, (16) image sensor.

(b)

Figure 5. Experimental configuration of 5D-ICOACH. (a) Schematic of the experimental setup (b) photograph of the experimental setup.

$\lambda = 530$ nm and $\Delta\lambda = 35$ nm, Newton, MA, USA) was collimated by a refractive lens (L1) with a focal length of 7.5 cm. Iris1 was used to control the initial beam illumination. This collimated beam passes through a linear polarizer (P1), which was used to switch the polarization state from '$\varphi = 0$' to '$\varphi = \pi/2$', and vice versa. The polarization state '$\varphi = 0$' refers to polarization along the active axis of the SLM, and the polarization state '$\varphi = \pi/2$' indicates that the polarization is orthogonal to the active axis of the SLM. A pinhole/object was critically illuminated using a converging lens (L2) with a focal length of 5 cm. Digits '2' and '3' from Group-2 of R1DS1N—Negative 1951 USAF Test Target, Ø1", were used as two objects. A pinhole of 100 μm was used to record the I_{PSF}. Light from the pinhole/object was then collected by a collimating lens (L3) with a focal length of 5 cm and an iris2. The collimated beam was incident on the SLM

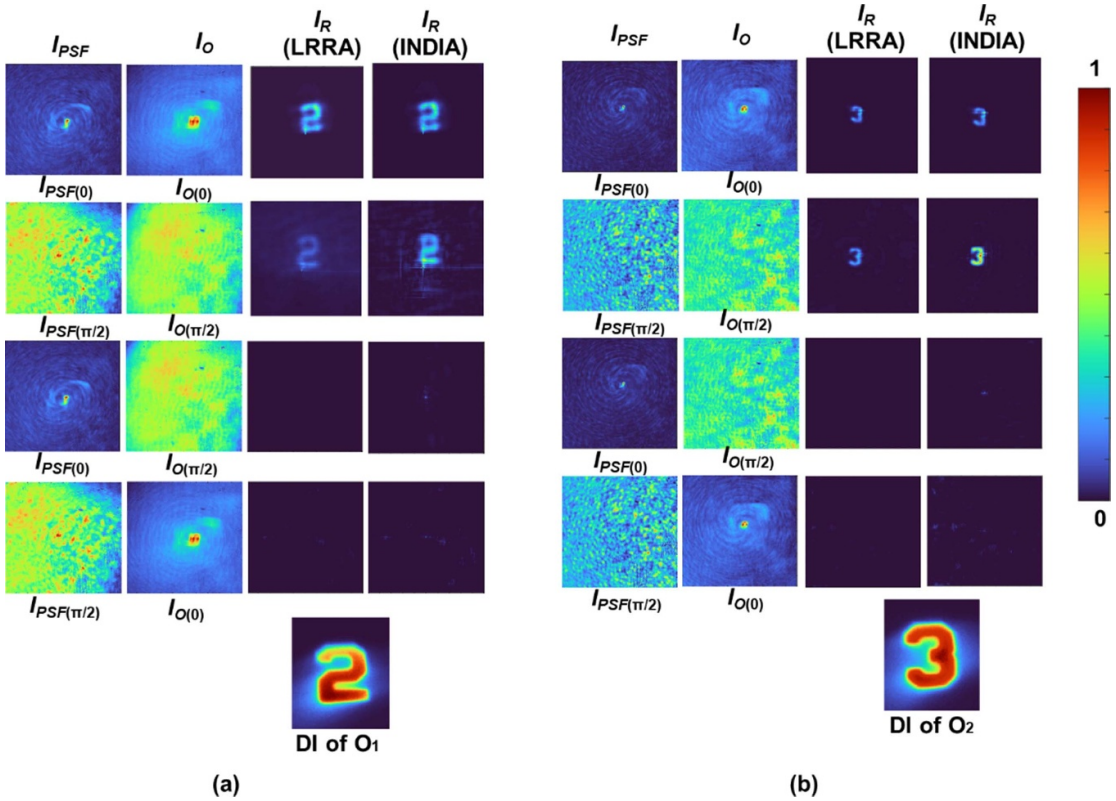

Figure 6. Polarization-sensitive I-COACH. (a) For O_1 in plane 1 ($z_s = 5$ cm). The I_{PSF} (C1) and I_O (C2) at two polarization states, 0 and $\pi/2$. Corresponding reconstruction results using the LRRA (C3) and the INDIA (C4). (b) For O_2 at $z_s = 6$ cm. The I_{PSF} (C1) and recorded I_O (C2) at two polarization states (0 and $\pi/2$). Corresponding reconstruction results using the LRRA (C3) and the INDIA (C4). (C: column, R: row, DI: Direct image).

(Thorlabs Exulus-4K 1/M, 3840 × 2160 pixels, pixel size = 3.74 μm, Newton, MA, USA) through a beam splitter (BS). A SLs with a topological charge ($L = 5$), as in the simulation study in section 3, was displayed on the SLM. The light reflected from the SLM was projected onto the fabricated QRDL through a 4-f imaging system consisting of two refractive lenses (L4 and L5) with focal lengths of 7.5 and 10 cm, respectively, with a demagnification factor of 0.75. It should be noted that the best light modulation can be obtained for polarization along the active axis of the SLM, and there is no modulation at the orthogonal polarization state to the active axis of the SLM. This characteristic has been utilized to experimentally demonstrate the polarization switchability in I-COACH by using two phase masks (SL and QRDL). For the '$\varphi = 0$' polarization state, both diffractive functions are activated, resulting in a complex modulation function, and for '$\varphi = \pi/2$', only amplitude modulation is activated. The I_{PSF} and I_O at two polarization states, '$\varphi = 0$ and $\pi/2$', were recorded with an image sensor (Zelux CS165MU/M 1.6 MP monochrome CMOS camera, 1440 × 1080 pixels with a pixel size of ~3.5 μm; Newton, MA, USA). Like any I-COACH system, as long as misalignments do not form between recording an I_{PSF} and I_O, the reconstruction results will not be affected. The 4F projection system between the SLM and the QRDL mimics an I-COACH system with a single element between the object and the image sensor enabling a high stability.

6. Results and discussion

6.1. Polarization imaging in I-COACH

In the first step, an experiment was carried out to demonstrate polarization-dependent I-COACH. The point spread intensity distribution (I_{PSF}) and response-to-object intensity distribution (I_O) were recorded for a pinhole (100 μm) and objects O_1 (digit '2') and O_2 (digit '3') at two polarization states (0 and $\pi/2$) and at two depths ($z_s = 5$ cm and $z_s = 6$ cm), respectively. Figure 6(a) shows the recorded I_{PSF} (column 1) and recorded I_O (column 2) at two polarization states, 0 and $\pi/2$, respectively. The corresponding reconstruction results are shown for the LRRA (column 3) and INDIA (column 4). Similarly, figure 6(b) shows the recorded I_{PSF} (column 1) and recorded I_O (column 2) for O_2 at two polarization states, 0 and $\pi/2$. The corresponding reconstruction results are shown for the LRRA (column 3) and INDIA (column 4) in figure 6(b). The results corresponding to I_{PSF} and I_O at the same polarization states [$I_{PSF}(0)I_O(0)$ and $I_{PSF}(\pi/2)I_O(\pi/2)$] show that

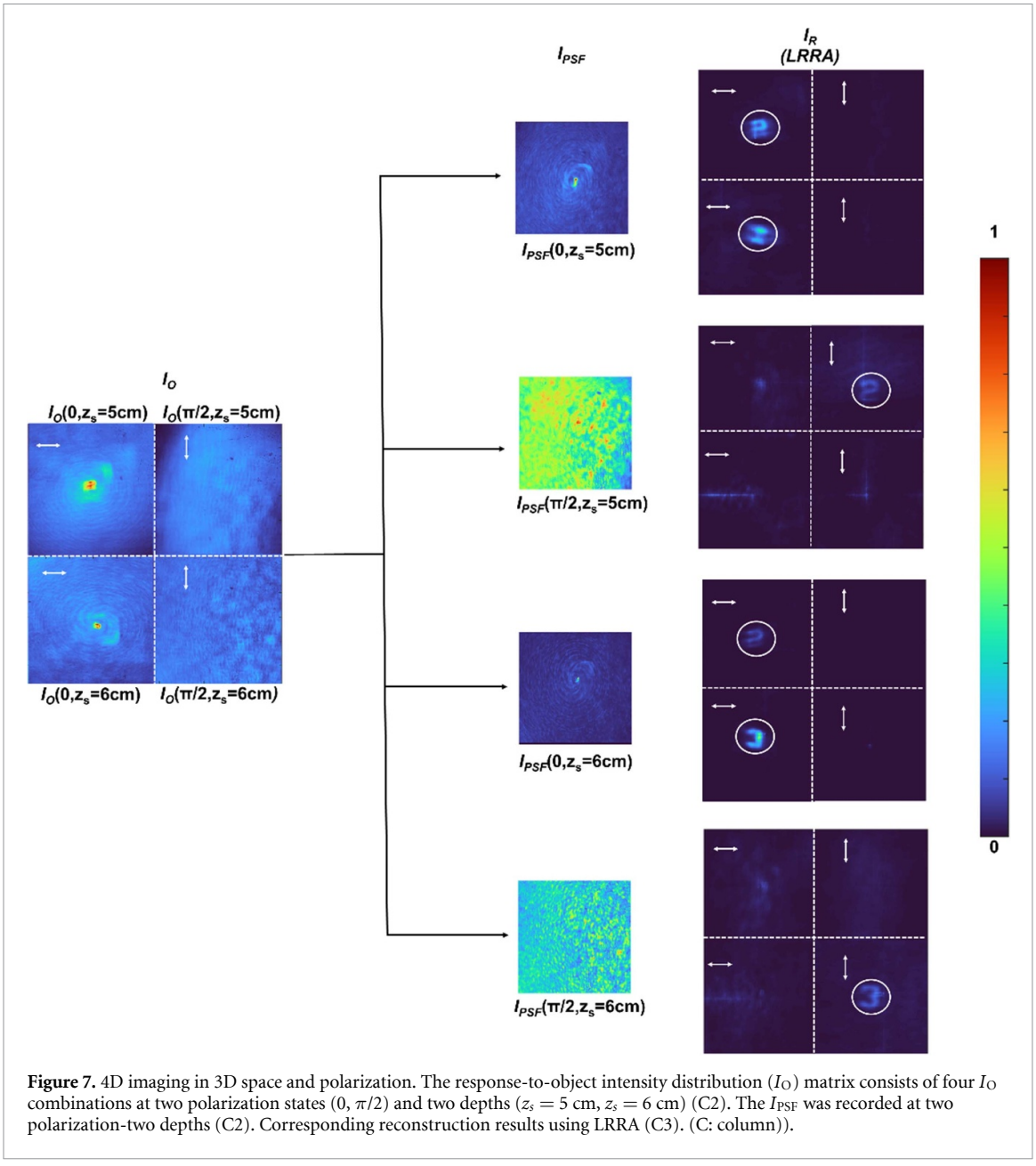

Figure 7. 4D imaging in 3D space and polarization. The response-to-object intensity distribution (I_O) matrix consists of four I_O combinations at two polarization states (0, $\pi/2$) and two depths ($z_s = 5$ cm, $z_s = 6$ cm) (C2). The I_{PSF} was recorded at two polarization-two depths (C2). Corresponding reconstruction results using LRRA (C3). (C: column)).

the image of the object has been reconstructed. For cross-polarization states [$I_{PSF}(0)I_O(\pi/2)$ and $I_{PSF}(\pi/2)I_O(0)$], the image of the object is not reconstructed.

6.2. 4D imaging in 3D space and polarization in I-COACH

The 4D imaging capabilities in 3D space and polarization were investigated in I-COACH. The results are shown in figure 7. In figure 7, the results are presented in three columns. The matrices of columns 1 and 3 consist of submatrices of order 2 × 2. In 4D I-COACH, I_O at two polarization states and two depths were stitched computationally into a single matrix of order 2 × 2 and reconstructed with recorded I_{PSF} at different polarization states (0 and $\pi/2$) and two different planes with a separation of 1 cm longitudinally. The first column of figure 8 illustrates the computationally stitched synthetic matrix, with four recordings, i.e. $I_O(0, z_s = 5$ cm), $I_O(\pi/2, z_s = 5$ cm), $I_O(0, z_s = 6$ cm) and $I_O(\pi/2, z_s = 6$ cm), and column 2 of figure 8 represents the recorded I_{PSF}s, i.e. $I_{PSF}(0, z_s = 5$ cm), $I_{PSF}(\pi/2, z_s = 5$ cm) $I_{PSF}(0, z_s = 6$ cm) $I_{PSF}(\pi/2, z_s = 6$ cm). The corresponding reconstruction results obtained using LRRA are shown in column 3 of figure 8. It is evident from the reconstruction results (column 3, rows 1 and 3) that for polarization state 0, objects at both planes are recovered from the point spread intensity distribution at plane 1, i.e. $I_{PSF}(0, z_s = 5$ cm). Similar results were obtained for the point spread intensity distribution at plane 2, i.e. $I_{PSF}(0, z_s = 6$ cm). Rows 2 and 4 of column 3 show the reconstruction results for polarization state $\pi/2$. Figure 7 clearly shows that the reconstruction of object images with I_{PSF}s of orthogonal polarization states is not possible. However, the

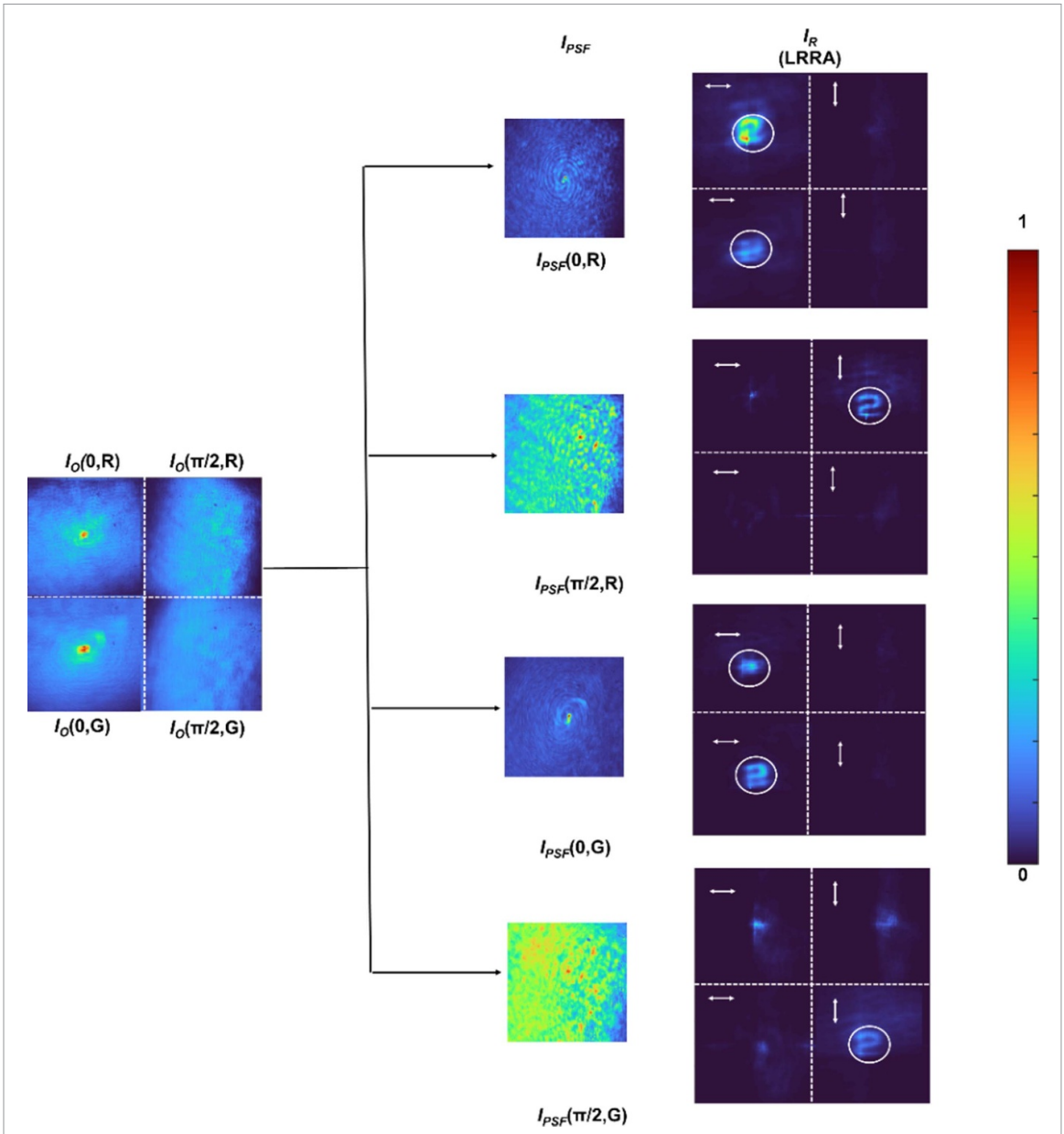

Figure 8. 4D imaging along 2D space, spectrum and polarization. The response-to-object intensity distribution (I_O) matrix consists of four recordings of I_O at two polarization states (0, $\pi/2$) and two wavelengths (G, R) (C1). The I_{PSF}*s* at two polarization states and two wavelengths (C2) were recorded. The corresponding reconstruction results obtained using LRRA are shown in (C3). (C: column, G: green, R: red).

reconstruction of object images with I_{PSF}*s* of different depths causes only blurring. The reconstruction of O_1 in row 1 of column 3 is sharper than the reconstruction of O_1 in row 3 of column 3. Similarly, the reconstruction of O_2 in row 3 of column 3 is sharper than the reconstruction of O_2 in row 1 of column 3.

6.3. 4D imaging in 2D space, wavelength and polarization in I-COACH

In the next step, 4D imaging in 2D space, spectra and polarization were investigated in I-COACH. The experiment was repeated with red LED Thorlabs (940 mW, $\lambda = 660$ nm and $\Delta\lambda = 33$ nm; Newton, MA, USA), and the corresponding I_{PSF} and I_O were recorded with the image sensor. The same recording procedure was repeated for the green LED. To demonstrate 4D imaging, different experimental recordings of response-to-object intensity distributions (I_O) at two wavelengths, i.e. green (G) and red (R), and two polarization states, i.e. 0 and $\pi/2$, were computationally stitched into a single matrix and reconstructed with recorded I_{PSF}s at orthogonal polarization states and the above two wavelengths. Figure 8 shows the 4D imaging results of I-COACH along the 2D space, spectrum and polarization orientations. In figure 8, the results are presented in three columns. The matrices of columns 1 and 3 consist of submatrices of order 2×2. The first column of figure 8 depicts the computationally stitched synthetic submatrix of the response-to-object intensity distribution, consisting of four recordings, i.e. I_O(0,R), I_O(π/2,R), I_O(0,G), and

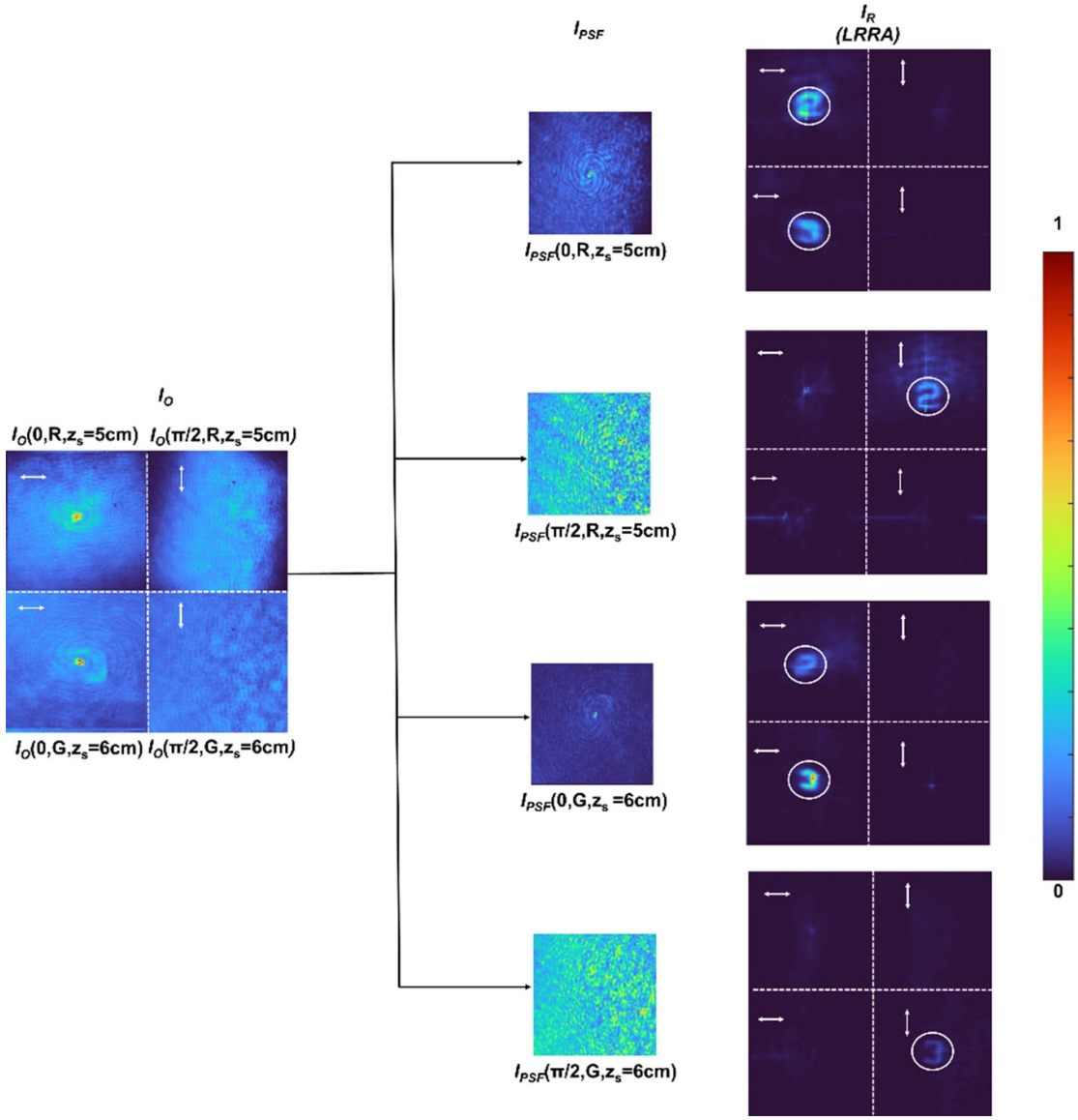

Figure 9. 5D imaging along 3D space, spectrum and polarization. The response-to-object intensity distribution (I_O) matrix consists of four I_O recordings at two polarization states (0, $\pi/2$), two depths ($z_s = 5$ cm and $z_s = 6$ cm), and two wavelengths (G, R) (C1). The I_{PSF} was recorded at different polarization states, depths and wavelengths (C2). Corresponding reconstruction results using LRRA (C3). (C: column, G: green, R: red).

$I_O(\pi/2,G)$, and column 2 of figure 8 represents the recorded I_{PSF}s, i.e. $I_{PSF}(0,R)$, $I_{PSF}(\pi/2,R)$, $I_{PSF}(0,G)$ and $I_{PSF}(\pi/2,G)$. The corresponding reconstruction results obtained using LRRA are shown in column 3 of figure 8. Column 3 consists of 4 submatrices of order 2×2, which illustrates the reconstruction corresponding to submatrix in column 1. Figure 9 clearly shows that the $I_{PSF}s$ of the green LEDs recovered the object information recorded with the red LED and vice versa, as demonstrated in previous I-COACH studies [28]. However, when the polarization state is not matched, there is no image reconstruction, indicating strong polarization discrimination.

6.4. 5D imaging along 3D space, spectrum and polarization in I-COACH

In the final experiment, 5D imaging along 3D space, spectrum and polarization was investigated. The 5D imaging results of I-COACH are provided in figure 9. In figure 9, the results are presented in three columns. The matrices of columns 1 and 3 consist of submatrices of order 2×2. In 5D I-COACH, different combinations of I_O at two polarization states (0 and $\pi/2$), two depths ($z_s = 5$ cm and $z_s = 6$ cm, $\Delta z = 1$ cm), and two wavelengths (G and R) are computationally stitched into a single submatrix of order 2×2 such that each element of this matrix represents different combinations of five dimensions. For example, the first element of this combined matrix, i.e. $I_O(0, R, z_s = 5$ cm), indicates the recorded response-to-object intensity distribution at the 0 polarization state with red light at plane 1 of $z_s = 5$ cm. This 5D response-to-object

intensity distribution was reconstructed from the recorded I_{PSF}at two orthogonal polarization states, two depths, and two wavelengths. The first column of figure 10 shows the computationally stitched synthetic matrix, consisting of four recordings, i.e. I_O (0, R, $z_s = 5$ cm), I_O ($\pi/2$, R, $z_s = 5$ cm), I_O (0, G, $z_s = 6$ cm), and I_O ($\pi/2$, G, $z_s = 6$ cm), and column 2 of figure 9 represents the recorded I_{PSF}s, i.e. I_{PSF} (0, R, $z_s = 5$ cm), I_{PSF} ($\pi/2$, R, $z_s = 5$ cm), I_{PSF} (0, G, $z_s = 6$ cm), and I_{PSF} (0, G, $z_s = 6$ cm). The corresponding reconstruction results obtained using LRRA are shown in column 3 of figure 9. Column 3 consists of 4 submatrices of order 2×2, which illustrates the reconstruction corresponding to submatrix in column 1. Figure 9 shows that depth specific, wavelength specific and polarization specific information can be retrieved from a single recording. The discrimination along depth is only mild, resulting in a slight blur, whereas the discrimination along wavelength and polarization is strong, resulting in no image of the object for the current conditions.

7. Conclusion and future perspectives

In this study, 5D imaging along 3D space, spectrum and polarization in I-COACH is proposed and experimentally demonstrated for the first time. This 5D imaging has been achieved using a single camera shot, which allows us to implement the idea at the same speed as the recording of any commercial image sensor. Therefore, in principle, 5D I-COACH can be expanded to 6D I-COACH for recording 5D information in real time. Like the previous I-COACH techniques [28], a calibration step is required where the PSF library is recorded along all three parameters, namely, depth, wavelength and polarization. This technique leverages the polarization-dependent light modulation capability of SLM using two-phase masks (SL, QRDL) by switching the polarization to orthogonal states. The study was carried out in various steps. First, I-COACH was experimentally demonstrated for polarization-dependent image reconstructions using LRRA. As expected, better reconstruction results were obtained for similar polarization states than for orthogonal polarization states due to the high intensity correlation for similar polarization states, unlike cross-polarization states. In the next step, the technique was used to independently study 4D recording and reconstruction, i.e. polarization depth and polarization wavelength. The corresponding results indicate that it is possible to recover object information in one dimension from the PSF recorded at that dimension for a fixed polarization state. In the final step, 5D I-COACH was demonstrated by inter-connecting all five dimensions in a single frame, and image recovery was attempted from different configurations of I_{PSF} along 5D using the LRRA.

This study is the first attempt to connect the five dimensions in IDH. However, there are some challenges and bottlenecks associated with the proposed technique as well. The major disadvantage is the low signal-to-noise ratio (SNR) in comparison to that of previous IDH-based polarization imaging approaches [38, 39]. The artifacts seen in the experimental results of figures 6–9 are common reconstruction noises which can be minimized by optimizing the diffractive functions and developing advanced reconstruction algorithms. In the reconstruction results of figures 7–9, for certain cross reconstruction cases, the object information is visible and blurred and for certain cases, the object information is weaker than the background. This difference is based on the strength of the cross-correlation signal. When the intensity distribution varies mildly between two states of polarization, spectrum or depth, then the cross-correlation value is strong resulting in a blurred reconstruction yet strong. However, when the intensity distribution varies significantly between two state of polarization, spectrum or depth then the cross-correlation value decreases to the level of the background. The average value of SNR in this study is $\sim$32 dB and the light throughput is approximately 10% due to polarizer, BS, and amplitude type DOE. This is the penalty for improving the temporal resolution by an order in comparison to previous studies [38, 39]. Moreover, few anomalies are also observed in reconstruction results, such as the figure 8, the image reconstructed with nonmatching wavelength is almost completely disappear rather than being blurred. However, this challenge can be addressed in the future by finding the optimal diffractive element pairs to achieve a high SNR.

Furthermore, advanced computational reconstruction methods and deep learning methods may be applied to improve the SNR of the current results. Another point we believe that needs to be mentioned is that the current study has been reported only for two polarization states that are orthogonal. We believe that this study can be expanded to include other polarization orientations in the future. The developed and demonstrated 5D I-COACH may be a useful tool for birefringence microscopy and functional and structural imaging applications [41].

Data availability statement

All data that support the findings of this study are included within the article (and any supplementary files).

Acknowledgments

We thank Professor Etienne Brasselet (University of Bordeaux, CNRS, Laboratoire Ondes et Matière d'Aquitaine, Talence F-33400, France) for useful discussions on this work.

This research was funded by European Union's Horizon 2020 research and innovation programme Grant Agreement No. 857627 (CIPHR); This work was partly supported by the European Regional Development Fund under Grant 1.1.1.5/19/A/003; Israel Innovation Authority (79555, MAGNET); Discovery Grant DP240103231 from Australian Research Council. Fabrication process was conducted using the NAMUR+ core facility funded by the Estonian Research Council (TT 13).

ORCID iDs

Narmada Joshi https://orcid.org/0009-0004-3826-7816
Vipin Tiwari https://orcid.org/0000-0002-2467-8225
Tauno Kahro https://orcid.org/0000-0002-8243-902X
Tatsuki Tahara https://orcid.org/0000-0001-9560-1041
Aarne Kasikov https://orcid.org/0000-0003-0850-4927
Kaupo Kukli https://orcid.org/0000-0002-5821-0364
Saulius Juodkazis https://orcid.org/0000-0003-3542-3874
Aile Tamm https://orcid.org/0000-0002-0547-0824
Joseph Rosen https://orcid.org/0000-0002-9739-2180
Vijayakumar Anand https://orcid.org/0000-0001-8867-1949

References

[1] Vijayakumar A and Rosen J 2017 Interferenceless coded aperture correlation holography–a new technique for recording incoherent digital holograms without two-wave interference *Opt. Express* **25** 13883–96
[2] Rosen J, Vijayakumar A, Kumar M, Rai M R, Kelner R, Kashter Y, Bulbul A and Mukherjee S 2019 Recent advances in self-interference incoherent digital holography *Adv. Opt. Photonics* **11** 1–66
[3] Rosen J *et al* 2021 Roadmap on recent progress in FINCH technology *J. Imaging* **7** 197
[4] Tahara T *et al* 2022 Roadmap of incoherent digital holography *Appl. Phys.* B **128** 193
[5] Javidi B *et al* 2021 Roadmap on digital holography *Opt. Express* **29** 35078–118
[6] Rosen J and Brooker G 2007 Digital spatially incoherent Fresnel holography *Opt. Lett.* **32** 912–4
[7] Kim M K 2012 Adaptive optics by incoherent digital holography *Opt. Lett.* **37** 2694–6
[8] Kelner R and Rosen J 2012 Spatially incoherent single channel digital Fourier holography *Opt. Lett.* **37** 3723–5
[9] Ables J G 1968 Fourier transform photography: a new method for x-ray astronomy *Publ. Astron. Soc. Aust.* **1** 172–3
[10] Dicke R H 1968 Scatter-hole cameras for x-rays and gamma rays *Astrophys. J.* **153** L101–L6
[11] Richardson W 1972 Bayesian-based iterative method of image restoration *J. Opt. Soc. Am.* **62** 55–59
[12] Lucy L B 1974 An iterative technique for the rectification of observed distributions *Astron. J.* **79** 745–54
[13] Horner J L and Gianino P D 1984 Phase-only matched filtering *Appl. Opt.* **23** 812–6
[14] Rai M R, Vijayakumar A and Rosen J 2018 Non-linear adaptive three-dimensional imaging with interferenceless coded aperture correlation holography (I-COACH) *Opt. Express* **26** 18143–54
[15] Wan Y, Liu C, Ma T, Qin Y and lv S 2021 Incoherent coded aperture correlation holographic imaging with fast adaptive and noise-suppressed reconstruction *Opt. Express* **29** 8064–75
[16] Zhang M, Wan Y, Man T, Zhang W and Zhou H 2024 Non-iterative reconstruction of interferenceless coded aperture correlation holography enabled high quality three-dimensional imaging *Opt. Lasers Eng.* **173** 107929
[17] Anand V, Han M, Maksimovic J, Ng S H, Katkus T, Klein A, Bambery K, Tobin M J, Vongsvivut J and Juodkazis S 2022 Single-shot mid-infrared incoherent holography using Lucy-Richardson-Rosen algorithm *Opto-Electron. Sci.* **1** 210006
[18] Rosen J and Anand V 2024 Incoherent nonlinear deconvolution using an iterative algorithm for recovering limited-support images from blurred digital photographs *Opt. Express* **32** 1034–46
[19] Antipa N, Kuo G, Heckel R, Mildenhall B, Bostan E, Ng R and Waller L 2018 DiffuserCam: lensless single-exposure 3D imaging *Optica* **5** 1–9
[20] Singh A K, Pedrini G, Takeda M and Osten W 2017 Scatter-plate microscope for lensless microscopy with diffraction limited resolution *Sci. Rep.* **7** 10687
[21] Linda Liu F, Kuo G, Antipa N, Yanny K and Waller L 2020 Fourier DiffuserScope: single-shot 3D Fourier light field microscopy with a diffuser *Opt. Express* **28** 28969–86
[22] Rai M R and Rosen J 2019 Noise suppression by controlling the sparsity of the point spread function in interferenceless coded aperture correlation holography (I-COACH) *Opt. Express* **27** 24311–23
[23] Liu C, Man T and Wan Y 2022 High-quality interferenceless coded aperture correlation holography with optimized high SNR holograms *Appl. Opt.* **61** 661–8
[24] Xavier A P I, Arockiaraj F G, Gopinath S, John Francis Rajeswary A S, Reddy A N K, Ganeev R A, Singh M S A, Tania S D M and Anand V 2023 Single shot 3D incoherent imaging using deterministic and random optical fields with Lucy-Richardson-Rosen algorithm *Photonics* **10** 987
[25] Adams J K *et al* 2022 *In vivo* lensless microscopy via a phase mask generating diffraction patterns with high-contrast contours *Nat. Biomed. Eng.* **6** 617–28
[26] Sahoo S K, Tang D and Dang C 2017 Single-shot multispectral imaging with a monochromatic camera *Optica* **4** 1209–13
[27] Vijayakumar A and Rosen J 2017 Spectrum and space resolved 4D imaging by coded aperture correlation holography (COACH) with diffractive objective lens *Opt. Lett.* **42** 947–50

[28] Anand V, Ng S H, Maksimovic J, Linklater D, Katkus T, Ivanova E P and Juodkazis S 2020 Single shot multispectral multidimensional imaging using chaotic waves *Sci. Rep.* **10** 13902
[29] Monakhova K, Yanny K, Aggarwal N and Waller L 2020 Spectral DiffuserCam: lensless snapshot hyperspectral imaging with a spectral filter array *Optica* **7** 1298–307
[30] Solomon J E 1981 Polarization imaging *Appl. Opt.* **20** 1537–44
[31] Treibitz T and Schechner Y Y 2009 Active polarization descattering *IEEE Trans. Pattern Anal. Mach. Intell.* **31** 385–99
[32] Wang J *et al* 2022 Linear polarization holography *Opto-Electron. Sci.* **1** 210009
[33] Zang J, Fan F, Liu Y, Wei R and Tan X 2019 Four-channel volume holographic recording with linear polarization holography *Opt. Lett.* **44** 4107–10
[34] Sheng W, Liu Y, Yang H, Shi Y and Wang J 2021 Polarization-sensitive imaging based on incoherent holography *Opt. Express* **29** 28054–65
[35] Jiao S and Ruggeri M 2008 Polarization effect on the depth resolution of optical coherence tomography *J. Biomed. Opt.* **13** 060503
[36] Chi W, Chu K and George N 2006 Polarization coded aperture *Opt. Express* **14** 6634–42
[37] Tian X, Liu R, Wang Z and Ma J 2022 High quality 3D reconstruction based on fusion of polarization imaging and binocular stereo vision *Inf. Fusion* **77** 19–28
[38] Tahara T 2023 Polarization-filterless polarization-sensitive polarization-multiplexed phase-shifting incoherent digital holography (P4IDH) *Opt. Lett.* **48** 3881–4
[39] Tahara T 2024 Incoherent digital holography with two polarization-sensitive phase-only spatial light modulators and reduced number of exposures *Appl. Opt.* **63** B24–B31
[40] Gerchberg R W and Saxton W O 1972 A practical algorithm for the determination of phase from image and diffraction plane pictures *Optik* **35** 227–46
[41] Hitzenberger C K, Goetzinger E, Sticker M, Pircher M and Fercher A 2001 Measurement and imaging of birefringence and optic axis orientation by phase resolved polarization sensitive optical coherence tomography *Opt. Express* **9** 780–90